

GALAXIES

Strong damped Lyman- α absorption in young star-forming galaxies at redshifts 9 to 11

Kasper E. Heintz^{1,2,*}, Darach Watson^{1,2}, Gabriel Brammer^{1,2}, Simone Vejlgard^{1,2}, Anne Hutter^{1,2}, Victoria B. Strait^{1,2}, Jorrit Matthee³, Pascal A. Oesch^{4,1,2}, Páll Jakobsson⁵, Nial R. Tanvir⁶, Peter Laursen^{1,2}, Rohan P. Naidu⁷, Charlotte A. Mason^{1,2}, Meghana Killi^{1,2}, Intae Jung⁸, Tiger Yu-Yang Hsiao⁹, Abdurro'uf^{9,8}, Dan Coe^{8,9}, Pablo Arrabal Haro¹⁰, Steven L. Finkelstein¹¹, Sune Toft^{1,2}

Primordial neutral atomic gas, mostly composed of hydrogen, is the raw material for star formation in galaxies. However, there are few direct constraints on the amount of neutral atomic hydrogen (H I) in galaxies at early cosmic times. We analyzed James Webb Space Telescope (JWST) near-infrared spectroscopy of distant galaxies, at redshifts ≥ 8 . From a sample of 12 galaxies, we identified three that show strong damped Lyman- α absorption due to H I in their local surroundings. The galaxies are located at spectroscopic redshifts of 8.8, 10.2, and 11.4, corresponding to 400 to 600 million years after the Big Bang. They have H I column densities $\geq 10^{22} \text{ cm}^{-2}$, which is an order of magnitude higher than expected for a fully neutral intergalactic medium, and constitute a gas-rich population of young star-forming galaxies.

Galaxy formation begins when primordial neutral atomic hydrogen (H I) accretes into dark matter halos, cools, and then forms stars (1, 2). Determining the accretion and build-up of H I gas in the earliest galaxies is therefore necessary to understand the first phases of galaxy formation. Galaxies at redshift $z \approx 8$ are thought to produce ionizing radiation that reionizes the intergalactic medium (3); however, the amount of ionizing radiation that escapes typical galaxies is thought to depend on their H I content. The weak 21-cm radio emission line of H I can only be observed for nearby galaxies, preventing direct detection of H I emission at cosmological distances (4, 5).

Alternatively, H I can be observed at high redshifts through its ultraviolet Lyman- α ($\text{Ly}\alpha$) absorption line, which appears in the spectra of bright background point sources, such as quasars or the optical afterglows of gamma-ray bursts (6, 7). $\text{Ly}\alpha$ absorbers with H I column densities $N_{\text{H I}} \geq 2 \times 10^{20} \text{ cm}^{-2}$ are known as damped $\text{Ly}\alpha$ absorbers (DLAs), because the absorption line appears with broad damping

wings. Observations of DLAs have shown extended, dense H I gas reservoirs surrounding star-forming galaxies (6) but only probe narrow pencil-beam sightlines. Dense H I gas that covers the ultraviolet emission of entire galaxies and thereby produces DLAs is only observed in the most intensely ionized nearby galaxies at $z \approx 0$ with low metal content (8) or in more distant star-forming galaxies at $z \approx 3$ with similar physical properties, but very rarely with $N_{\text{H I}} > 5 \times 10^{21} \text{ cm}^{-2}$ (9). The large H I column densities of DLAs mean that the neutral gas is optically thick to ionizing photons. There are no DLA observations at redshifts ≥ 8 , when the Universe was being reionized and the first galaxies formed.

Spectroscopic observations

We examined previously published near-infrared James Webb Space Telescope (JWST) spec-

troscopy of 12 galaxies (table S1) to search for DLAs. These galaxies were selected because they are at $z > 8$, determined from at least two detected emission lines, and have a median signal-to-noise ratio > 3 per resolution element in the wavelength region covering the $\text{Ly}\alpha$ line. We searched their spectra for a drop in flux with slow rollover redward of the expected position of the $\text{Ly}\alpha$ line, which would indicate damping-wing absorption. To avoid contamination by the neutral gas in the intergalactic medium (IGM), we required any candidate DLA to exceed the expected IGM column density by at least 2σ confidence (10). We found that three of the galaxies meet these criteria.

Two of these galaxies were identified as high-redshift galaxy candidates based on photometry (11–13) and designated CEERS-43833 and CEERS-16943. Both were subsequently confirmed using spectroscopy and had their redshifts measured as $z = 8.7622$ and 11.41, respectively, using the prism mode of the Near Infrared Spectrograph (NIRSpec) (14) on the JWST (15); we adopted these spectroscopic data in our analysis. The third source, designated MACS0647-JD, is gravitationally lensed by the foreground galaxy cluster MACS J0647+7015 and was also identified as a high-redshift galaxy candidate using photometry (16). Follow-up JWST imaging and spectroscopy showed that it has two distinct components (A and B), which are each multiply imaged by the gravitational lens (17). A NIRSpec prism observation of component A has shown that it is a star-forming galaxy at $z = 10.17$, on the basis of the identification of seven emission lines (18); we adopted these data for our analysis. Table 1 lists the celestial coordinates and redshifts of these three galaxies.

We downloaded the raw JWST spectroscopic and imaging data and then reduced them using the GRIZLI and MSAEXP software

Table 1. Properties of the three galaxies at $z = 9$ to 11 with detected DLAs. Celestial coordinates use the J2000 equinox. The uncertainties are reported at 1σ confidence. The O_{32} ionization parameter was not determined for CEERS-16943 because the $[\text{O III}] \lambda 5008$ line is redshifted out of the NIRSpec prism wavelength coverage.

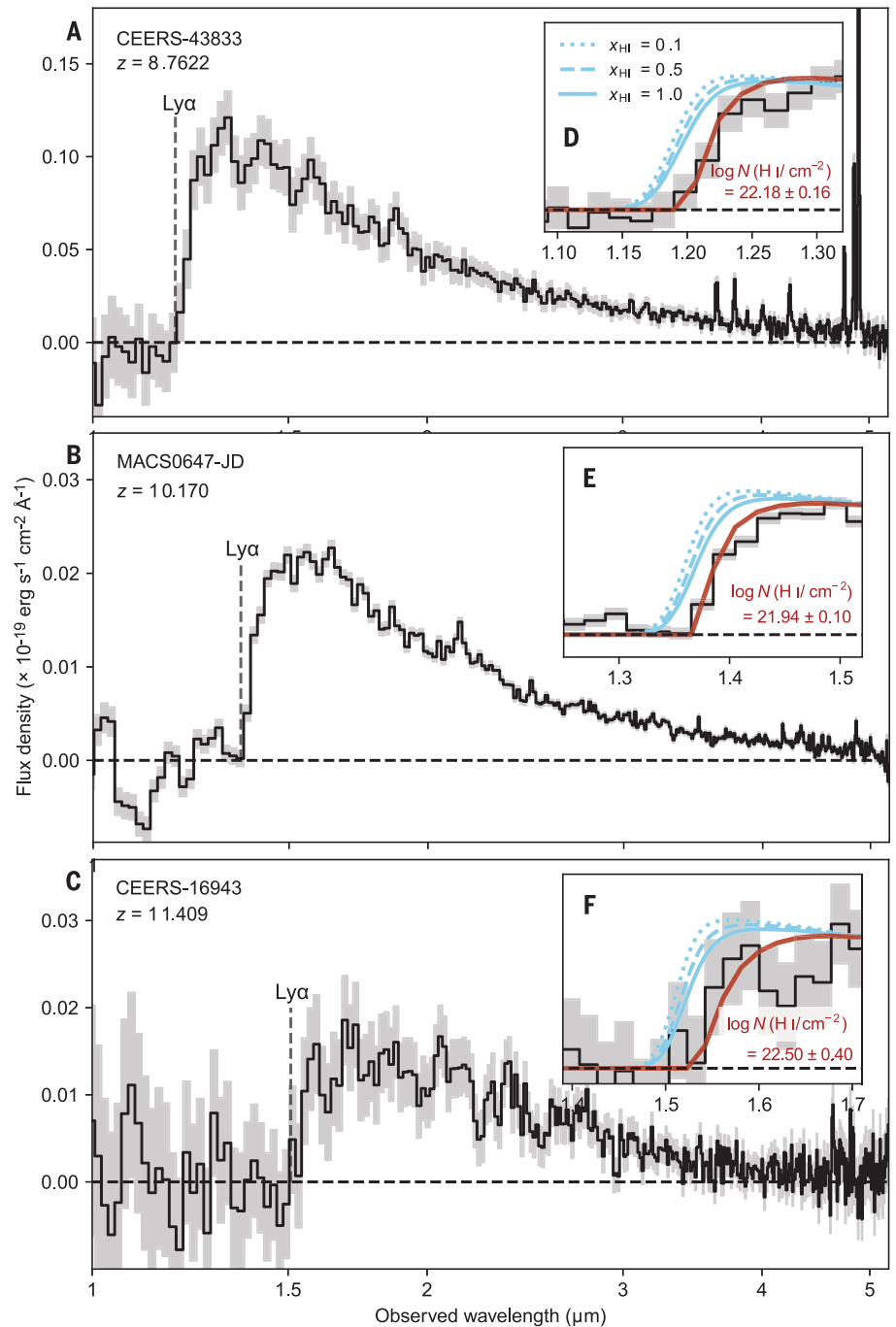
| Parameter | CEERS-43833 | MACS0647-JD | CEERS-16943 |
|--|---|---|---|
| Right ascension | 14 ^h 19 ^m 45 ^s .27 | 06 ^h 47 ^m 53 ^s .12 | 14 ^h 19 ^m 46 ^s .36 |
| Declination | +52°54'42" 3 | +70°14'22" 98 | +52°56'32" 8 |
| z | 8.7622 \pm 0.0004 | 10.170 \pm 0.003 | 11.409 \pm 0.001 |
| $\log(N_{\text{H I}}/\text{cm}^{-2})$ | 22.18 \pm 0.16 | 21.94 \pm 0.10 | 22.50 \pm 0.40 |
| $12 + \log[\text{O}/\text{H}]$ | 7.46 \pm 0.09 | 7.40 \pm 0.30 | 7.70 \pm 0.30 |
| $\text{SFR}/(M_{\odot} \text{ year}^{-1})$ | 14.5 ^{+14.4} _{-7.2} | (1.40 \pm 0.20)* | 4.30 ^{+4.20} _{-2.10} |
| O_{32} | 11.4 \pm 1.7 | (30.0 \pm 6.0)* | – |
| $\log(M_{\star}/M_{\odot})$ | 8.72 \pm 0.03 | (8.10 \pm 0.30)* | 8.90 \pm 0.08 |

*Value adopted from previous work (18).

¹Cosmic Dawn Center, Copenhagen, Denmark. ²Niels Bohr Institute, University of Copenhagen, DK-2200 Copenhagen N, Denmark. ³Institute of Science and Technology Austria, 2400 Klosterneuburg, Austria. ⁴Observatoire de Genève, Université de Genève, CH-1290 Versoix, Switzerland. ⁵Centre for Astrophysics and Cosmology, Science Institute, University of Iceland, Reykjavik, Iceland. ⁶School of Physics and Astronomy, University of Leicester, LE1 7RH Leicester, UK. ⁷Kavli Institute for Astrophysics and Space Research, Massachusetts Institute of Technology, Cambridge, MA 02139, USA. ⁸Space Telescope Science Institute, Baltimore, MD 21218, USA. ⁹Center for Astrophysical Sciences, Department of Physics and Astronomy, The Johns Hopkins University, Baltimore, MD 21218, USA. ¹⁰National Optical-Infrared Astronomy Research Laboratory, National Science Foundation, Tucson, AZ 85719, USA. ¹¹Department of Astronomy, The University of Texas at Austin, Austin, TX 78712, USA.

*Corresponding author. Email: keheintz@nbi.ku.dk

Fig. 1. Near-infrared spectra of three high-redshift galaxies with DLAs. (A to C) The photometrically calibrated NIRSpec prism spectra covering 1 to 5.2 μm (black) are plotted with their associated 1σ uncertainties (gray) for (A) CEERS-43833; (B) MACS0647-JD, demagnified assuming a magnification factor of $\mu = 8 \pm 1$ (18); and (C) CEERS-16943. The dashed vertical line indicates the expected position of the Ly α line, given the redshift measured from longer-wavelength emission lines. (D to F) Insets of (A) to (C) show zoomed-in views of the region around the Ly α transition and model data for comparison. We show the theoretical expectation for varying neutral IGM H I fractions, $x_{\text{HI}} = 0.1$, 0.5, or 1.0 (blue dotted, dashed, and solid lines, respectively), and the best-fitting models with an additional DLA feature (red), all convolved with the spectral resolution. A strong DLA with $\log(N_{\text{H I}}/\text{cm}^{-2}) \geq 22.0$ is detected in all three cases.



tools (10, 19, 20). We scaled and matched the optimally extracted one-dimensional (1D) spectra to the available JWST photometry [from the Near Infrared Camera (NIRCam)] using a wavelength-dependent polynomial function (10), determined to optimize the absolute flux calibration and account for potential spectroscopic slit losses. Figure 1, A to C, shows the reduced and photometrically calibrated 1D spectra of the three galaxies at $z = 8.8$ to 11.4. We measured the redshifts from emission lines in the spectra (10) and confirmed the

values found by previous analyses of the same data (15, 18).

Modeling of the spectra

To model the intrinsic galaxy emission spectra, we used a set of galaxy templates (21) that were designed to reproduce the rest-frame ultraviolet colors of galaxies at $z > 8$. These templates were convolved with the spectral resolution of the NIRSpec prism (14). To account for the expected foreground absorption by the IGM, we modeled the optical depth of

the Ly α line due to the increasingly neutral IGM at increasing redshifts (22). We included an additional absorption-line component that describes the optical depth due to Ly α absorption from the interstellar medium (ISM) within each galaxy, or gas in the immediate surroundings of the galaxy (10).

The best fitting models (Fig. 1, D to F) have ISM neutral hydrogen column densities of $\log(N_{\text{H I}}/\text{cm}^{-2}) = 22.18 \pm 0.16$ for CEERS-43833, 22.50 ± 0.40 for CEERS-16943, and 21.94 ± 0.10 for MACS0647-JD. The uncertainties are the

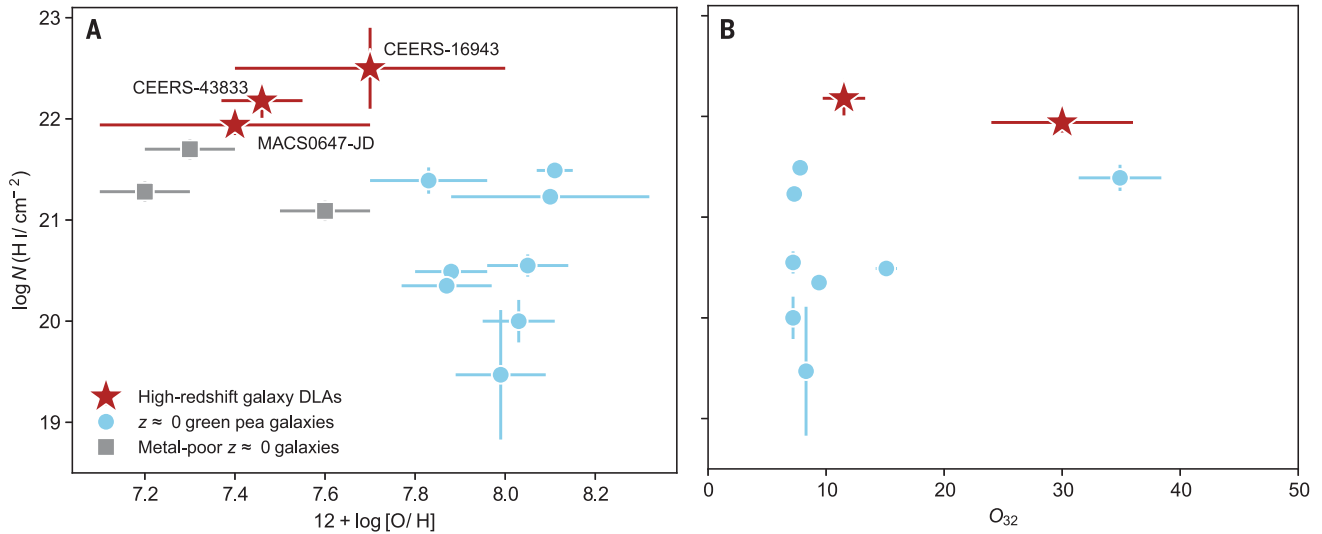


Fig. 2. H I column density relations with oxygen abundance and ionization.

(A and B) The measured H I column densities of the three $z \approx 9$ to 11 galaxies with DLAs (red stars) compared with $z \approx 0$ green pea galaxies (blue circles) (8) and three metal-poor galaxies at $z \approx 0$ (gray squares) (27) as a function of

(A) gas-phase oxygen abundance and (B) oxygen ionization, quantified by the O_{32} parameter. The high-redshift star-forming galaxies have the highest H I column density. Error bars show 1σ confidence intervals, which, in some cases, are smaller than the symbol sizes.

16th to 84th percentiles of the posterior probability distributions from the fitting process and include a systematic uncertainty of 0.1 dex (decimal exponent) due to variations in the galaxy templates. The models are not very sensitive to the value of the neutral hydrogen fraction in the IGM ($x_{\text{H I}}$) because the line profiles of the DLAs dominate the optical depth at the resonance frequency of the Ly α line. Figure 1, D to F, shows models with $x_{\text{H I}} = 0.1$, 0.5, and 1.0 (corresponding to 10, 50, and 100% neutral IGM) convolved with the spectral resolution (the effect of this convolution is shown in fig. S5). We found that none of these simple IGM models reproduce the broad absorption features observed in the JWST spectra, and so we ruled out that all the Ly α absorption arises from the IGM, even in the case of a fully neutral IGM. This indicates that the excess Ly α absorption is due to abundant H I gas in the ISM of these galaxies.

We also considered an alternative scenario in which the DLA absorption could be caused by a largely neutral IGM that contains overdensities close to each galaxy. The overdensities required at this epoch would be a factor of 30 to 50 times larger than the average volumetric IGM H I gas density, which is approaching galaxy ISM densities, so we regard this explanation as unlikely. An overdensity has previously been reported in one of the larger JWST survey fields at $z \sim 8.7$ (23, 24), which is at least five times the field average for very bright galaxies, too small an enhancement to explain our observed absorption. Figure S7 shows Ly α transmission curves derived from cosmological simulations (25) that include a

wide range of distributions representing variations in the density fields around the set of simulated galaxies at $z \approx 8.8$ (see supplementary text). We found that none of these models reproduce the observed broad DLA features either.

We also considered, but excluded, scenarios involving nebular continuum emission and two-photon processes as the cause of the damped Ly α profiles (see supplementary text). Figure S6 compares the spectrum of CEERS-43833 to the spectra of three galaxies at $z \approx 9$ that passed our data-quality cuts but have no evidence of DLA absorption. The comparison galaxies do not have similar broad absorption features in their spectra, though they are consistent with the models with substantial IGM neutral fractions. Figure S6 also compares the observed spectra to the intrinsic IGM and DLA models convolved with the spectral resolution (which varies with wavelength). We found that the spectral resolution is not responsible for the width of the observed Ly α line profiles. Having excluded the possibility that the observed DLAs arise from IGM absorption, we therefore ascribed the DLAs to H I gas located in the immediate surroundings of each of the three galaxies.

Physical properties of the galaxies

To investigate the physical properties of the three galaxies, we measured the line fluxes of each emission line detected in the spectra. For CEERS-43833, we detected (with $>3\sigma$ significance) the emission lines [O II] $\lambda 3727$ (where the λ notation indicates the line rest wavelength in angstroms), [O III] $\lambda\lambda 4960, 5008$, He I $\lambda 3889$, and the Balmer lines H β , H γ , and H δ .

For MACS0647-JD, we recovered the same emission lines as in previous work (18), including [O II] $\lambda 3727$, [O III] $\lambda 4363$, [Ne III] $\lambda 3870$, He I $\lambda 3889$, and the Balmer lines H γ and H δ . For CEERS-16943, we detected [O II] $\lambda 3727$, [Ne III] $\lambda 3870$, and He I $\lambda 3889$. To determine the line fluxes, we used a model consisting of Gaussian line profiles, superimposed on the best-fitting continuum from the galaxy template. Our model assumes that all emission lines in a single galaxy have the same redshift and line widths, but the line fluxes are free parameters. The measured line fluxes are reported in table S2.

We used the H β (for CEERS-43833) or [O II] $\lambda 3727$ (for MACS0647-JD and CEERS-16943) line-flux measurements to derive the star-formation rates (SFRs) of the galaxies (10), which we found to be in the range of 1 to $15 M_{\odot} \text{ year}^{-1}$ (where M_{\odot} is the mass of the Sun). From a set of strong-line diagnostics calibrated to the strongest emission lines, we measured logarithmic oxygen abundances for the galaxies of $12 + \log [\text{O}/\text{H}] = 7.4$ to 7.7 (10), which is 5 to 10% of the Sun's oxygen abundance. There is weak evidence, which is not statistically significant ($<3\sigma$), for absorption lines of Si IV $\lambda 1397$ and C IV $\lambda 1550$ in CEERS-43833 at the same redshift as the nebular emission lines. However, we cannot determine whether these highly ionized absorption lines are associated with the DLA. We fitted a stellar population model to the spectral energy distribution (SED) of the three galaxies (10) and found that they all have young (≤ 100 million years old) stellar populations with total stellar masses $M_{\star} = 10^8$ to $10^9 M_{\odot}$. The physical

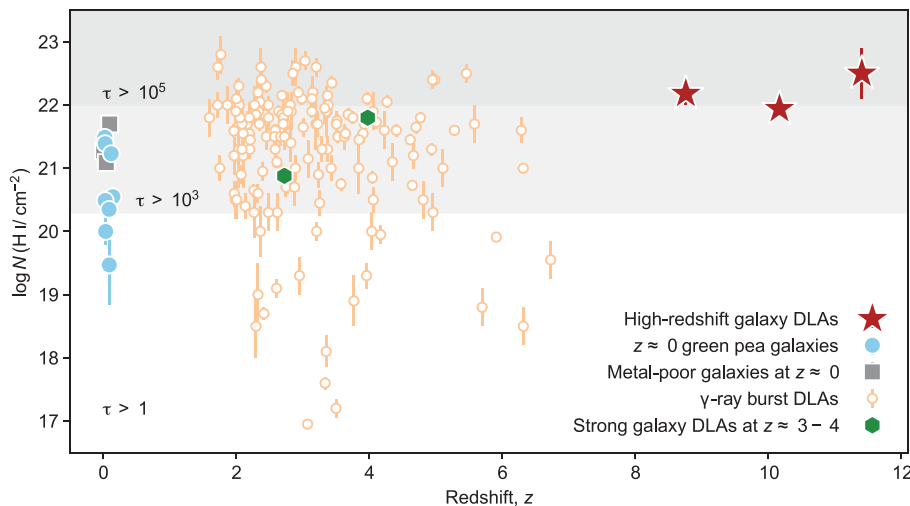


Fig. 3. H I column density measured at different redshifts. The same objects (with the same symbols) as in Fig. 2 but plotted as a function of redshift. For comparison, we also show star-forming galaxies at $z \approx 3$ to 4 with the strongest DLAs (31, 32) (green hexagons) and gamma-ray burst Ly α absorbers at $z \approx 2$ to 6 (7) (orange open circles). The light gray region indicates $N_{\text{H I}} > 2 \times 10^{20} \text{ cm}^{-2}$, which is the minimum required for a DLA. The dark gray region indicates $N_{\text{H I}} > 10^{22} \text{ cm}^{-2}$, which corresponds to an optical depth $\tau > 10^5$ at the Lyman limit. Error bars show 1σ confidence intervals, which, in some cases, are smaller than the symbol sizes.

properties of these three galaxies are summarized in Table 1; they are consistent with the observed population of star-forming galaxies at $z = 7$ to 10 (26) (fig. S3).

Comparison with other DLA systems

We compared the properties of these three high-redshift galaxies to a group of metal-poor nearby galaxies at $z \approx 0$, called green pea galaxies, which are sometimes considered lower-redshift analogs of high-redshift galaxies (8). Figure 2 shows the H I column density of these $z \approx 0$ emission-line galaxies as functions of their oxygen abundances and ionization parameter $O_{32} \equiv [\text{O III}] \lambda 5008 / [\text{O II}] \lambda 3727$. This figure also shows data for the lowest metallicity galaxies known: Zw I 18, SBSG 0335–052, and SBSG 1415+437 (27). The three galaxies at $z = 9$ to 11 have substantially higher H I column densities than any of the local high-redshift analog galaxies, even at similar metallicities (Fig. 2A). We found that the galaxies with high ionization parameters in general also show larger H I column densities. Theoretical predictions and previous empirical results (28, 29) have shown that higher Ly α emission equivalent widths and higher escape fractions, and thereby lower H I column densities, are expected from galaxies with higher O_{32} ratios. The strong absorption of Ly α , corresponding to optical depths (τ) of $>10^5$ (30), in these three high-redshift galaxies might be due to their young stellar populations, which have not yet had time to substantially ionize even their local surroundings before initiating the large-scale IGM reionization.

Figure 3 compares our measured H I column densities to the above samples of metal-poor, $z \approx 0$ high-redshift analog galaxies (8, 27) and gamma-ray burst Ly α absorbers (7), the latter population probing the most extreme absorption-selected galaxy distribution. Figure 3 also includes two DLAs in star-forming galaxies at $z \approx 3$ to 4 (31, 32), which are a rare population of galaxies at that epoch (9). Our results extend the observed population of DLAs to higher redshifts and are among the strongest DLA systems known (Fig. 3).

The H I column densities we derived for the high-redshift galaxies indicate that the H I gas is opaque to ionizing photons, owing to self-shielding. This implies negligible escape fractions of ionizing photons along our line of sight. If the DLA features in these galaxies are related to viewing angle effects, such as observing along unusually gas-rich sightlines, other low-column density channels might exist and be responsible for the high O_{32} values that we measured from the emission lines. Such strongly directionally dependent escape of ionizing radiation has been found in simulations (33–35). We used the DLA measurements to place lower bounds on the H I gas masses of the three galaxies. Assuming a spherical geometry and deriving the physical sizes of the galaxies based on their imaging (10), the total H I gas masses are $M_{\text{H I}} \approx 10^{8.5}$ to $10^9 M_{\odot}$. These values are consistent with those predicted by the Astraeus simulation (see supplementary text). These H I masses are roughly two to seven times higher than the inferred stellar masses, and the gas depletion times to star

formation are 1 to 50 million years. Our measured SFRs of the $z = 9$ to 11 star-forming galaxies are at the high end of the SFR surface densities (Σ_{SFR}) observed in the local Universe (36). However, their inferred gas surface densities (Σ_{gas}) are offset toward lower values compared with the relation describing Σ_{SFR} as a function of Σ_{gas}^n , where n is an empirical scaling index (36) (see supplementary text). This likely indicates that the assumption of spherical symmetry that we made above provides only lower limits on the galaxies' total gas masses, given the empirical universality of this relation.

Implications for galaxy assembly and reionization

Our results provide a direct measurement of neutral atomic H I gas reservoirs in the local environments of galaxies during the onset of the large-scale reionization of the IGM at $z > 8$. Previous work had found circumstantial evidence for abundant neutral gas reservoirs in early galaxies, on the basis of singly ionized ultraviolet absorption lines (37) or larger Ly α damping wing profiles than expected from simple models of a neutral IGM (18, 38). Far-infrared observations of gas in high-redshift galaxies have indirectly indicated similarly abundant H I gas reservoirs (39, 40), which have also been deduced from the lower metal content of high-redshift galaxies, indicating dilution of the heavier element abundances (26). We found three DLAs from a sample of 12 galaxies, and so we inferred that strong damped Ly α absorption is common in galaxies at $z = 9$ to 11; such systems are scarce in star-forming galaxies at intermediate redshifts $z \approx 3$ (9).

To maintain the large H I column densities while being spatially extended over the physical size of the galaxy, these sources must be surrounded by massive, extended sheets or shells of neutral gas. We suggest that these DLA galaxy systems might be particularly prevalent in the era during which the large-scale IGM was reionized, at least at $z > 8$. Consequently, galaxies like these are likely to have low escape fractions of ionizing photons owing to the high H I column densities and extensive gas covering fractions, at least at their observed evolutionary stages. We expect that the damping wings caused by the neutral gas in the IGM are masked by the large H I abundance in the local environment of these galaxies; if they are common at that epoch, this effect could cause overestimations of the neutral hydrogen fraction in the IGM (41).

REFERENCES AND NOTES

1. D. Kereš, N. Katz, D. H. Weinberg, R. Davé, *Mon. Not. R. Astron. Soc.* **363**, 2 (2005).
2. J. Schaye et al., *Mon. Not. R. Astron. Soc.* **402**, 1536–1560 (2010).
3. D. P. Stark, *Annu. Rev. Astron. Astrophys.* **54**, 761–803 (2016).

4. X. Fernández *et al.*, *Astrophys. J. Lett.* **824**, L1 (2016).
5. N. Maddox *et al.*, *Astron. Astrophys.* **646**, A35 (2021).
6. A. M. Wolfe, E. Gawiser, J. X. Prochaska, *Annu. Rev. Astron. Astrophys.* **43**, 861–918 (2005).
7. N. R. Tanvir *et al.*, *Mon. Not. R. Astron. Soc.* **483**, 5380–5408 (2019).
8. J. H. McKinney *et al.*, *Astrophys. J.* **874**, 52 (2019).
9. A. E. Shapley, C. C. Steidel, M. Pettini, K. L. Adelberger, *Astrophys. J.* **588**, 65–89 (2003).
10. Materials and methods are available as supplementary materials.
11. S. L. Finkelstein *et al.*, *Astrophys. J. Lett.* **940**, L55 (2022).
12. S. L. Finkelstein *et al.*, *Astrophys. J. Lett.* **946**, L13 (2023).
13. M. B. Bagley *et al.*, *Astrophys. J. Lett.* **946**, L12 (2023).
14. P. Jakobsen *et al.*, *Astron. Astrophys.* **661**, A80 (2022).
15. P. Arrabal Haro *et al.*, *Nature* **622**, 707–711 (2023).
16. D. Coe *et al.*, *Astrophys. J.* **762**, 32 (2013).
17. T. Y.-Y. Hsiao *et al.*, *Astrophys. J. Lett.* **949**, L34 (2023).
18. T. Y.-Y. Hsiao *et al.*, arXiv:2305.03042 [astro-ph.GA] (2023).
19. G. Brammer, grizli. Zenodo (2023); <https://doi.org/10.5281/zenodo.7767790>.
20. G. Brammer, msaexp: NIRSpec analysis tools. Zenodo (2022); <https://doi.org/10.5281/zenodo.7299500>.
21. R. L. Larson *et al.*, arXiv:2211.10035 [astro-ph.GA] (2023).
22. X. Fan *et al.*, *Astron. J.* **132**, 117–136 (2006).
23. E. Leonova *et al.*, *Mon. Not. R. Astron. Soc.* **515**, 5790–5801 (2022).
24. L. Whitler *et al.*, *Mon. Not. R. Astron. Soc.* **529**, 855–872 (2024).
25. P. Laursen, J. Sommer-Larsen, B. Milvang-Jensen, J. P. U. Fynbo, A. O. Razoumov, *Astron. Astrophys.* **627**, A84 (2019).
26. K. E. Heintz *et al.*, *Nat. Astron.* **7**, 1517 (2023).
27. S. Hernandez *et al.*, *Astrophys. J.* **892**, 19 (2020).
28. H. Yang *et al.*, *Astrophys. J.* **844**, 171 (2017).
29. A. E. Jaskot, T. Dowd, M. S. Oey, C. Scarlata, J. McKinney, *Astrophys. J.* **885**, 96 (2019).
30. H.-W. Chen, J. X. Prochaska, N. Y. Gnedin, *Astrophys. J.* **667**, L125–L128 (2007).
31. M. Pettini, C. C. Steidel, K. L. Adelberger, M. Dickinson, M. Giavalisco, *Astrophys. J.* **528**, 96–107 (2000).
32. X. Lin *et al.*, *Astrophys. J. Lett.* **944**, L59 (2023).
33. R. Cen, T. Kimm, *Astrophys. J. Lett.* **801**, L25 (2015).
34. J. Rosdahl *et al.*, *Mon. Not. R. Astron. Soc.* **515**, 2386–2414 (2022).
35. J. Y. C. Yeh *et al.*, *Mon. Not. R. Astron. Soc.* **520**, 2757–2780 (2023).
36. R. C. Kennicutt Jr., N. J. Evans II, *Annu. Rev. Astron. Astrophys.* **50**, 531–608 (2012).
37. K. Boyett *et al.*, arXiv:2303.00306 [astro-ph.GA] (2023).
38. E. Curtis-Lake *et al.*, *Nat. Astron.* **7**, 622–632 (2023).
39. K. E. Heintz *et al.*, *Astrophys. J. Lett.* **934**, L27 (2022).
40. K. E. Heintz *et al.*, *Astrophys. J. Lett.* **944**, L30 (2023).
41. M. McQuinn, A. Lidz, M. Zaldarriaga, L. Hernquist, S. Dutta, *Mon. Not. R. Astron. Soc.* **388**, 1101–1110 (2008).

ACKNOWLEDGMENTS

We thank the reviewers for their insightful and constructive feedback. We also thank J. Fynbo and M. Dickinson for valuable and enlightening comments on the interpretations of the results. We acknowledge the work and effort of the CEERS collaboration in obtaining some of the observations and are grateful that their early data are publicly available. The Cosmic Dawn Center is funded by the Danish National Research Foundation under grant DNR140. This work is based on observations made with the NASA/ESA/CSA James Webb Space Telescope (JWST). The data were obtained from the Mikulski Archive for Space Telescopes at the Space Telescope Science Institute, which is operated by the Association of Universities for Research in Astronomy, Inc., under NASA contract NAS 5-03127 for JWST. **Funding:** K.E.H. acknowledges support from Carlsberg Foundation Reintegration Fellowship grant CF21-0103. A.H. acknowledges support from the VILLUM FONDEN under grant 37459. C.A.M. acknowledges support from the VILLUM FONDEN under grant 37459 and the Carlsberg Foundation under grant CF22-1322. N.R.T. was funded through Science and Technology Facilities Council (STFC) consolidated grant ST/W000857/1. R.P.N. acknowledges funding from JWST programs GO-1933 and GO-2279. R.P.N. was supported by the NASA Hubble Fellowship grant HST-HF2-51515.001-A awarded by the Space Telescope Science Institute, which is operated by the Association of Universities for Research in Astronomy under NASA contract NAS5-26555. P.A.O. received

funding from the Swiss State Secretariat for Education, Research, and Innovation (SERI) under contract number MB22.00072 and from the Swiss National Science Foundation (SNSF) through project grant 200020_207349. **Author contributions:** K.E.H. and D.W. drafted the manuscript and led the analysis. G.B. reduced the observations and extracted the spectra. S.V. performed the IGM and DLA modeling. A.H. provided and interpreted the Astraes simulations output. V.B.S. performed the SED modeling. J.M., P.A.O., P.J., N.R.T., P.L., R.P.N., C.A.M., M.K., I.J., T.Y.H., A., D.C., P.A.H., S.L.F., and S.T. contributed to the interpretation and analysis of the results. **Competing interests:** The authors declare no competing interests. **Data and materials availability:** The JWST spectroscopic data are available at the Mikulski Archive for Space Telescopes (MAST) (<https://mast.stsci.edu>) under program IDs DD-2750 and GO-1433 for the three selected galaxies; the IDs for the other galaxies we searched are listed in table S1. Our data analysis codes are archived at Zenodo (19, 20). The reduced spectroscopic data are available through the DAWN JWST Archive (DJA): https://s3.amazonaws.com/msaexp-nirspec/extractions/nirspec_graded.html under file names ceers-ddt-v1_prism-clear_2750_28.spec.fits for CEERS-43833, macsj0647-v1_prism-clear_1433_3593.spec.fits for MACS0647-JD, and ceers-ddt-v1_prism-clear_2750_1.spec.fits for CEERS-16943. The photometry is available at <https://dawn-cph.github.io/dja/imaging/v7/>. Our derived physical parameters are provided in Table 1, and measured line fluxes are provided in table S2. **License information:** Copyright © 2024 the authors, some rights reserved; exclusive licensee American Association for the Advancement of Science. No claim to original US government works. <https://www.science.org/about/science-licenses-journal-article-reuse>

SUPPLEMENTARY MATERIALS

[science.org/doi/10.1126/science.adj0343](https://doi.org/10.1126/science.adj0343)
Materials and Methods
Supplementary Text
Figs. S1 to S8
Tables S1 and S2
References (42–95)

Submitted 2 June 2023; accepted 22 March 2024
10.1126/science.adj0343